A facile and low-cost synthesis of granulated blast furnace slag-based cementitious material coupled with Fe_2O_3 catalyst for treatment of dye wastewater

Yao Jun Zhang[*], Li Cai Liu, Lu Lu Ni, Bing Li Wang

School of Materials and Mineral Resources, Xi'an University of Architecture and Technology, Xi'an 710055, PR China

ABSTRACT

A facile and low-cost route was used to synthesize a novel catalyst of alkali-activated granulated blast furnace slag-based cementitious material (ASCM) coupled with Fe_2O_3 by a three-step reaction of polymerization, ion exchange and impregnation. The FESEM and XRD results revealed that a high compressive strength ASCM with mean particle size about 50 nm was synthesized and Fe_2O_3 covered on ASCM surface in the form of clusters. The photoluminescence peak sharply decreases with increase of Fe_2O_3 content due to the recombination probabilities of photogenerated electron–hole pairs to be inhibited. The photocatalytic activities for degradation of Congo red (CR) dye were evaluated and the sample of ASCM loaded about 5 wt% Fe_2O_3 showed the highest degradation efficiency under UV irradiation. The photocatalytic degradation of CR in solution obeys second order reaction kinetics and a possible reaction mechanism is proposed.

© 2013 Elsevier B.V. All rights reserved.

1. Introduction

Granulated blast furnace slag (GBFS) is an industrial by-product from the manufacture of pig iron and predominately consists of calcium–magnesium aluminosilicate glass [1,2]. The slag in long-term stock not only occupies a great quantity of land, but gives rise to serious environmental pollutions. In order to promote the resources recycling and sustainable development of steel industry, it is necessary to adopt an advanced method for the high value-added utilization of GBFS. In recent years, tremendous effort is focused on the utilization of GBFS for the synthesis of alkali-activated granulated blast furnace slag-based cementitious materials (ASCM) due to low energy consumption, high mechanical strength, low permeability and high stability in aggressive environments [3–7]. Under the effect of alkaline activator, the vitreous structure in GBFS initially depolymerizes and then forms amorphous calcium (alumino) silicate hydrate [C(A)SH] gel. It is proposed that the skeleton of C(A)SH gel with negative charges is composed of SiO_4 and AlO_4 tetrahedra linked alternately by sharing all bridge oxygen atoms, and the negative charges are balanced by positive of Ca^{2+} and Na^+ [8,9]. It is considered that calcium silicate hydrate (CSH) is the major amorphous phase in alkali-activated GBFS with a low Ca/Si ratio of 0.98–1.1 [10–13] and aluminum is present in CSH gel as 4-coordination with an Al/Ca ratio of 0.16–0.25 [14–16]. Mercury intrusion porosimetry results revealed that the ASCM possesses porous structure of a higher mesopore pore volume and a lower capillary pore fraction [17–20]. Cho et al. [21] reported that the micropore volume (<5 nm) is about 78% of their total pore volume in alkali-activated slag pastes. In consideration of porosity, the matrix of ASCM has been successfully utilized in the incorporation and immobilization of radioactive wastes and toxic metals [22–24]. Besides, the cations of Na^+, K^+ and Ca^{2+} in the charge-balancing sites of skeleton can be displaced by ion-exchange. In our previous study, the Na^+ cation in alkali-activated steel slag-based Na,Ca-cementitious material was replaced by Ni^{2+} cation to generate Ni,Ca-cementitious material and was employed as a photocatalyst for degradation of methylene blue [25]. Sazama et al. [26] reported that Na^+ and K^+ cations in metakaolin-based Na-geopolymer and metakaolin-slag based K,Ca-geopolymer were replaced by Co and Cu cations to prepare the Co-geopolymer and Cu-geopolymer for the oxidation of decane and the selective catalytic reduction of NO_x.

In this paper, a novel catalyst of alkali-activated granulated blast furnace slag-based cementitious material loaded Fe_2O_3 was firstly synthesized by a three-step reaction of polymerization, ion exchange and impregnation, and was used as a photocatalyst for the degradation of Congo red dye. The purposes want: (1) to realize

* Corresponding author at: College of Material Science and Engineering, Xi'an University of Architecture and Technology, No. 13 Yan Ya Road, Xi'an 710055, PR China. Tel.: +86 29 82202467; fax: +86 29 85535724.
E-mail addresses: yaojzhang@yahoo.com.cn, zhangyaojun@xauat.edu.cn (Y.J. Zhang).

high value-added resource recycling of GBFS, (2) to design a catalyst with low cost, environment friendly and energy-saving characters, (3) to have excellent degradation efficiency for the wastewater of dye and (4) to make the catalyst with high compressive strength and easy to separate from suspension solution.

2. Experimental

2.1. Materials

The GBFS with a Blaine specific surface area of 508 m^2 kg^{-1} was provided by Long Steel Company. The main chemical components by weight percent are shown in Table 1. Iron nitrate nonahydrate (A.R.) and sodium metasilicate nonahydrate (A.R.) were purchased from Xi'an Chemical Reagent Company.

2.2. Synthesis of Na-cementitious material

The raw materials, GBFS, activator (Na$_2$SiO$_3$·9H$_2$O) and water, are in the mass ratio of GBFS/activator/water = 1:0.11:0.30. In a typical synthesis, 1500 g of GBFS was put into a net paste stirrer and then the aqueous solution of alkaline activator was poured into it. Subsequently, the mixture was sufficiently stirred for 2 min. The slurry was cast into a 40 mm × 40 mm × 160 mm triplicate iron mold to be compacted on the vibrating table, and then put into a standard curing box for 24 h. The samples were continuously cured at room temperature for additional 7 days after demolded, and then the samples sealed in thin plastic bags respectively, were cured at 65 °C for 24 h in a nitrogen atmosphere. The sample with compressive and flexural strengths of 86 MPa and 2 MPa respectively was crushed to obtain a Na-alkali-activated slag-based cementitious material (Na-ASCM) with particle size distribution from 0.125 to 0.315 mm.

2.3. Synthesis of ASCM loaded Fe$_2$O$_3$ catalyst

A weight of 160 g Na-ASCM was put into a 400 mL aqueous solution of 2.0 M NH$_4$Ac at room temperature for 24 h to carry out the ion exchange of Na$^+$ with NH$_4^+$. The sample was filtrated and washed adequately with deionized water, and then dried at 65 °C for 4 h in a nitrogen atmosphere. As described above, the ion exchange was repeated once more to get a NH$_4$-alkali-activated granulated blast furnace slag-based cementitious material (NH$_4$-ASCM).

The catalysts of ASCM loaded different amount of Fe$_2$O$_3$ were prepared by wetness impregnation. In a typical procedure for the fabrication of loading 0.5 wt% Fe$_2$O$_3$ sample, 30 g of NH$_4$-ASCM was impregnated with 15 mL of aqueous solution which dissolves 0.7587 g of Fe(NO$_3$)$_3$·9H$_2$O over night. The sample was dried at 65 °C for 12 h in a nitrogen atmosphere and then was calcinated at 300 °C for 3 h. The sample was assigned as 0.5Fe$_2$O$_3$/ASCM. According to the loading amount of 5 wt% and 10 wt% Fe$_2$O$_3$, the samples were designated as 5Fe$_2$O$_3$/ASCM and 10Fe$_2$O$_3$/ASCM, respectively. An accurate content of Fe$_2$O$_3$ in samples was analyzed by X-ray fluorescence analysis as shown in Table 1.

2.4. Analysis technique

Elemental Analysis was carried out on a Bruker S4 Pioneer X-ray fluorescence (XRF) analyzer. Thermogravimetric analysis (TGA), differential thermogravimetry (DTG) and differential scanning calorimetry (DSC) were conducted on a Mettler Toledo TGA/DSC 1 Stare system. X-ray diffraction patterns of samples were recorded on a D/MAX-2200 X-ray diffractometer equipped a rotation anode using CuKα radiation with a 0.02 2θ step interval. The morphology analysis was carried out on an S-4800 field emission scanning electron microscope. Diffuse reflectance UV–vis near infrared ray spectrum was recorded on a HITACHI UV-4100 spectrophotometer. The photoluminescence spectra were recorded on an F-4500 fluorescence spectrophotometer and a 150 W xenon lamp was used as excitation light source with an excitation wavelength of 250 nm. The compressive strength of sample was measured on a YAW-300 automatic pressure testing machine at loading speed of 2.4 kN s^{-1}. The flexural strength of sample was carried out on a DKZ-5000 anti-rupture testing machine with a three-point bend device at loading speed of 50 N s^{-1}. The N$_2$ adsorption–desorption isotherms were measured on an ASAP 2020 instrument. The TEM image of sample was obtained on an H-600 transmission electron microscopy.

2.5. Evaluation of photocatalytic activities

In different photocatalytic experiments, 0.2–0.4 g of catalyst was added to 100 mL of 2–10 mg L^{-1} aqueous Congo red (CR) solution. The reaction mixture was irradiated by a UV-lamp (ZW-2, 40 W) under magnetic stirring at room temperature, and was subsequently centrifuged in each 10–20 min interval. The absorbance of supernatant solution was monitored on a UV–vis spectrophotometer at the maximum absorption wavelength of 500 nm. The photocatalytic degradation rate (DR) was calculated by a formula (1).

$$DR = \left[\frac{A_0 - A_t}{A_0} \right] \times 100 \tag{1}$$

where DR is the degradation ratio of CR. The A_0 and A_t are the absorbency of CR solution in initial time and in t time after UV irradiation, respectively. In all of the adsorption experiments, the aqueous CR solution was put in the dark for certain times and then filtrated to measure the absorbance of supernatant solution at the maximum absorption wavelength of 500 nm.

3. Results and discussion

3.1. Structure characteristics of Fe$_2$O$_3$/ASCM catalyst

The chemical components of samples are shown in Table 1. The GBFS contains a certain amount of metallic and non-metallic oxides components. The contents of Na$_2$O and SiO$_2$ in GBFS are 0.57% and 27.51% respectively, but those values in the Na-ASCM sample increased to 4.45% and 31.11% respectively. After Na$^+$ ions are exchanged by NH^{4+} ions, the amount of Na$_2$O rapidly decreases to 0.14%, indicating that almost all of Na$^+$ ions in the matrix of Na-ASCM were displaced by NH$_4^+$ ions at room temperature. Sazama et al. [26] reported that the Na$^+$ ions in the geopolymer network could be exchanged by Cu^{2+} or Co^{2+} ions at room temperature. The transformation of Na-ASCM into NH$_4$-ASCM attempts to reduce the alkalinity of ASCM and to prevent from the generation of iron hydroxide precipitation in the process of wetness impregnation of Fe$_2$O$_3$.

Fig. 1 shows the thermoanalysis curves of TGA, DSC and DTG for the solid Fe(NO$_3$)$_3$·9H$_2$O. The weight loss in TGA curve can be divided into two steps. The weight loss in the first step is about 2.01% from room temperature to 108 °C with a maximum weight loss temperature of 87 °C in DTG and 3.80 J g^{-1} of endotherm in DSC due to the loss of a small quantity of free water. The weight loss in the second step is about 74.09% from 108 to 314 °C in TGA with a maximum weight loss temperature of 189 °C in DTG and 27.57 J g^{-1} of endotherm in DSC resulting from the thermal decomposition of solid Fe(NO$_3$)$_3$·9H$_2$O. So, this is the reason why the calcination temperature for the sample is selected to 300 °C.

Fig. 2 displays the X-ray diffraction patterns of samples. From the pattern of GBFS it can be found that there is a broad diffuse hump in the region of 20–38 2θ, suggesting that the GBFS predominantly

Table 1
Chemical components of samples (wt%).

| Components	Na_2O	Fe_2O_3	Al_2O_3	SiO_2	CaO	MgO	K_2O	TiO_2	MnO	BaO	SO_3	LOI
GBFS	0.57	1.03	10.59	27.51	35.23	7.11	0.66	1.16	0.48	0.38	1.41	13.87
Na-ASCM	4.45	1.12	8.91	31.11	31.48	5.74	0.61	1.06	0.43	0.37	1.23	13.49
NH_4-ASCM	0.14	1.17	11.27	34.04	26.72	7.10	0.31	1.28	0.49	0.36	0.80	16.32
$0.5Fe_2O_3$/ASCM	0.16	1.77	11.19	33.83	27.16	7.04	0.31	1.26	0.49	0.36	0.73	15.70
$5Fe_2O_3$/ASCM	0.15	6.22	10.75	33.72	26.97	6.12	0.3	1.18	0.46	0.36	0.68	13.09
$10Fe_2O_3$/ASCM	0.14	11.39	9.34	32.24	26.46	5.19	0.24	1.07	0.4	0.33	0.58	12.62
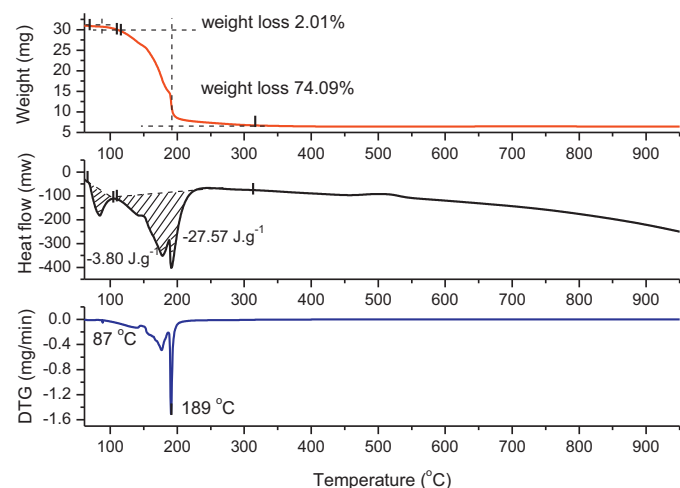
Fig. 1. Thermogravimetric analysis (TGA), differential scanning calorimetry (DSC) and differential thermogravimetry (DTG) for the iron nitrate nonahydrate.

possesses glassy phase. In comparison with the pattern of GBFS, the amorphous hump has remarkably shifted toward lower 2θ values in the pattern of NH_4-ASCM, indicating that the alkali-activated slag-based cementitious material is mainly X-ray amorphous materials [27]. Meanwhile, some small peaks superimposed on the amorphous hump at about $2\theta = 29.4°$, $32.1°$ are assigned to be the poorly crystalline phase of calcium silicate hydrate (CSH) (JCPDS No. 00-033-0306), and the peaks at about $2\theta = 11.4°$ and $31.3°$ are ascribed to the calcium aluminate hydrate (CAH) (JCPDS No. 02-0083). Wang et al. [12,28] reported that the CSH with low C/S ratio is predominate hydration product, and Mozgawa and Deja [9] confirmed that there are both CSH and CAH phases in the system of alkali-activated GBFS. It is observed from the pattern of $0.5Fe_2O_3$/ASCM sample that

there is no any new peak appearance, and one peak disappears at $2\theta = 11.4°$ by contrast to the pattern of Na-ASCM. It is worthy to note that the amorphous hump is further broadened and all of the peaks vanish with increase amount of Fe_2O_3 in the patterns of $5Fe_2O_3$/ASCM and $10Fe_2O_3$/ASCM, respectively, suggesting that a large number of Fe_2O_3 cover on the surfaces of CSH and CAH in the form of high dispersion clusters with particle size below the limit of XRD detectability [29] as comparison with the pattern of pure Fe_2O_3 (JCPDS No. 33-0664) synthesized by the decomposition of solid $Fe(NO_3)_3 \cdot 9H_2O$. Perera et al. [30] reported the speciation of iron in an MK-based geopolymer was present in octahedral coordination as isolated ions and no any crystalline Fe-rich phase was observed in the geopolymer.

The N_2 adsorption–desorption isotherms belong to the isotherms of type IV as shown in Fig. 3. The hysteresis loops in the relative pressure (P/P_0) region of 0.45–1.0 demonstrate that there are mesoporous structures. It can be estimated from the shape of isotherms that well-defined mesoporous characteristic is in the order of NH_4-ASCM > $5Fe_2O_3$/ASCM > $10Fe_2O_3$/ASCM > GBFS.

Table 2 lists some physical parameters of samples, such as BET Specific surface area, pore volume, average pore size and pore volume percentage. The GBFS sample has the quite small S_{BET} (10.63 m^2/g) and pore volume (0.034 mL/g). After Na-ASCM was carried out an ion exchange of Na^+ with NH_4^+ to form NH_4-ASCM, the S_{BET} (61.55 m^2/g), pore volume (0.16 mL/g) and mesoporous volume percentage (73.69%) have significantly increased compared to the GBFS sample, indicating that the NH_4-ASCM with inimitably mesoporous structure is beneficial to as a adsorbent for adsorption of CR molecule with 3D size of 3 nm × 0.25 nm × 0.73 nm. Li et al. [31] reported that synthesized alkali-activated fly ash binders exhibited much higher adsorption capacity than fly ash itself and natural zeolites. When different amounts of Fe_2O_3 are loaded on NH_4-ASCM, the parameters of pore volume, average pore size and pore volume percentage of 5–50 nm are obviously reduced due to

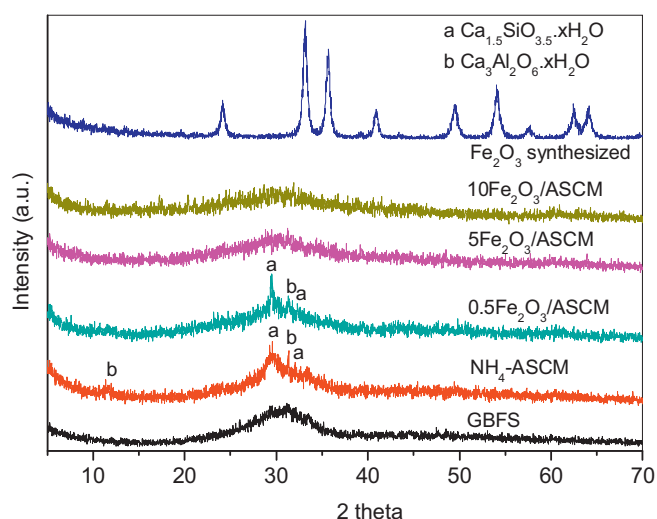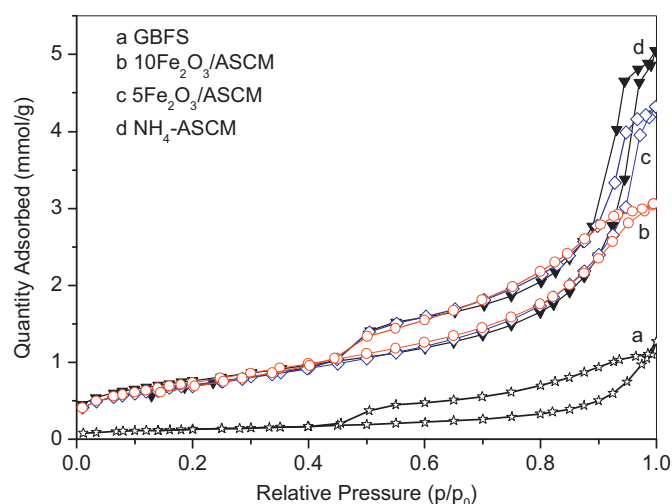**Fig. 2.** X-ray diffraction patterns of samples.

Fig. 3. N_2 adsorption–desorption isotherms of samples.

Table 2
BET specific surface area, pore volume, average pore size and pore volume percentage.

Sample	S_{BET} (m²/g)	Pore volume (mL/g)	Average pore size (nm)	Pore volume (%)		
				<5 nm	5–50 nm	>50 nm
GBFS	10.63	0.034	12.71	33.08	51.41	15.51
NH₄-ASCM	61.55	0.16	10.44	21.14	73.69	5.17
5Fe₂O₃/ASCM	57.76	0.14	9.48	26.92	69.17	3.91
10Fe₂O₃/ASCM	60.42	0.10	6.79	38.37	58.08	3.55

immobilization of Fe_2O_3 into channels and on surfaces as shown in Table 2.

Fig. 4 shows the images of field emission scanning electron microscope (FESEM) coupled with energy dispersive X-ray analysis (EDXA) for the $5Fe_2O_3$/ASCM sample. The morphology of the ASCM supporter is an aggregate of nanoparticles with mean particle size about 50 nm [27,32]. However, it is difficult to distinguish the particle size of Fe_2O_3 in Fig. 4a. By combining with XRD results in Fig. 2 it can be proposed that the Fe_2O_3 particles exist in the form of clusters. EDXA result presents that the $5Fe_2O_3$/ASCM sample is mainly composed of Al, Ca, Fe, Mg, Si and O elements in Fig. 4b. The elemental map in Fig. 4c shows that the Fe appears to be uniformly dispersed in the matrix of ASCM.

Fig. 5 shows the TEM image of $5Fe_2O_3$/ASCM sample. It can be seen that Fe_2O_3 molecules in the form of 3–5 nm clusters disperse on ASCM support. However, there is aggregation of clusters probably due to the limited surface area in Table 2 and nanoscale effect of small size particles.

Fig. 6 presents the diffuse reflectance UV–vis near infrared ray spectra of samples. It can be observed that the absorption edges in the range of 250–700 nm are gradually blue-shifted with the decrease of Fe content due to the quantum size effect. But the spectrum intensity decreases in order of $5Fe_2O_3$/ASCM < $10Fe_2O_3$/ASCM < $0.5Fe_2O_3$/ASCM < Na-ASCM in the near infrared region, especial for the peaks located at 1424 and 2221 nm as a consequence of the strong interaction between Fe_2O_3 clusters and ASCM.

Fig. 7 shows the photoluminescence spectra of samples excited by a 150 W xenon lamp with an excitation wavelength of 250 nm. All of the samples have a same emission peak at 399 nm. The Na-ASCM sample displays the highest peak deriving from the quick recombination of photogenerated electron–hole pairs. The photoluminescence peak decreases sharply with the increase amount of Fe_2O_3, implying that the transition frequency of photogenerated electrons is quickened up and the recombination probabilities of photogenerated electron–hole pairs are decreased in the interface of Fe_2O_3 clusters and ASCM due to the strong interaction between of Fe_2O_3 clusters and porous ASCM [33].

3.2. Photocatalytic degradation efficiency

3.2.1. Effect of catalyst dosage on degradation rate

The effect of $5Fe_2O_3$/ASCM catalyst dosage on degradation rate of CR is investigated under the conditions of the initial CR concentration of $8 \, mg \, L^{-1}$ in the volume of 100 mL as shown in Fig. 8. It is found that the degradation rate of CR increases with increasing of catalyst dosage, and 0.4 g of $5Fe_2O_3$/ASCM sample shows 100% degradation rate under UV irradiation for 100 min. This can be attributed to the increases in the number of Fe_2O_3 active sites on composite surface so that the photooxidation efficiency of CR is enhanced.

3.2.2. Effect of initial dye concentration on degradation rate

A series of CR solutions are employed to explore the effect of initial dye concentration on degradation rate of CR in a
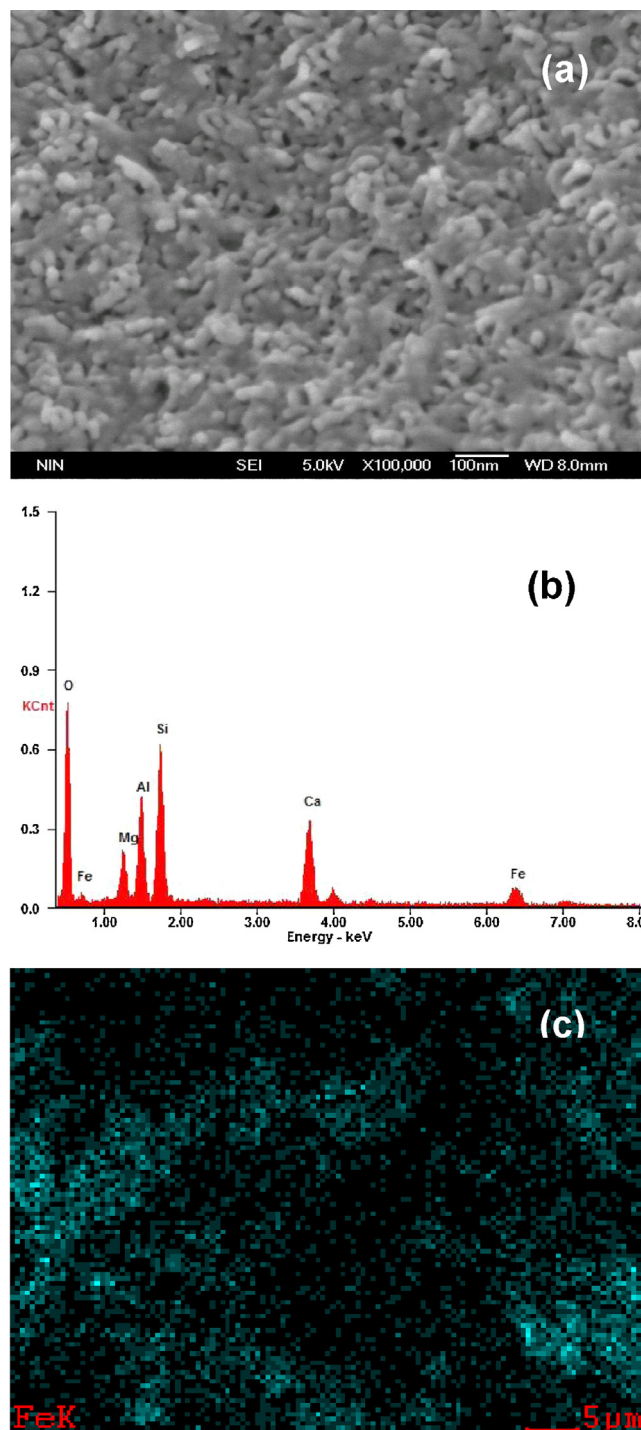

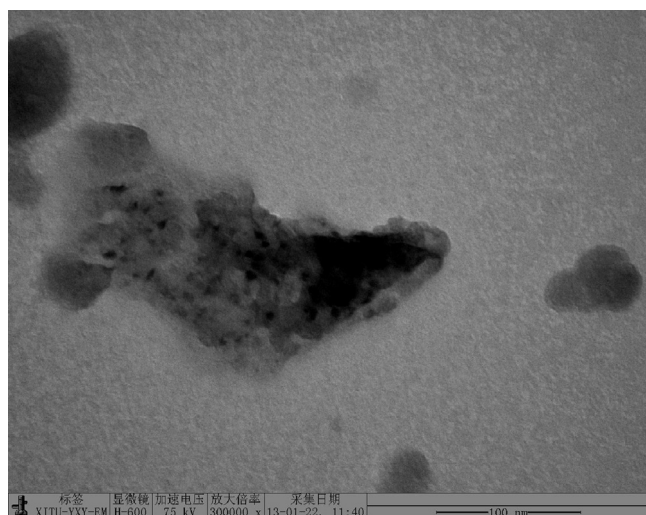**Fig. 4.** FESEM images coupled with EDXA for the $5Fe_2O_3$/ASCM sample. (a) FESEM image, (b) EDXA and (c) Fe elemental map.
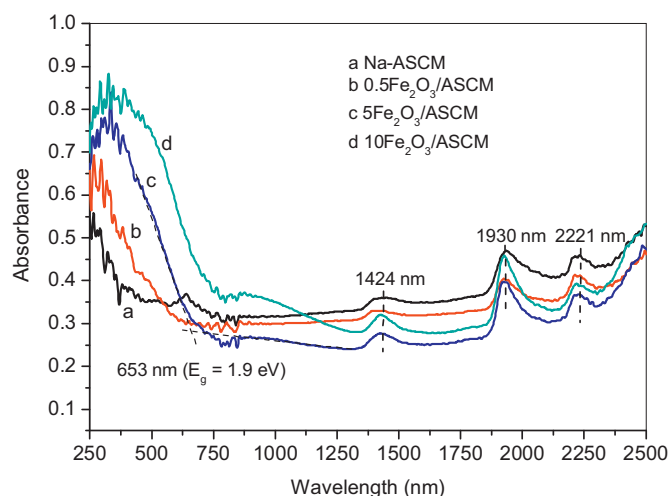
Fig. 5. TEM image of 5Fe$_2$O$_3$/ASCM sample.

Fig. 6. Diffuse reflectance UV–vis near infrared ray spectra of samples.

Fig. 7. Photoluminescence spectra of specimens excited by a 150 W xenon lamp with an excitation wavelength of 250 nm.

Fig. 8. Effect of 5Fe$_2$O$_3$/ASCM catalyst dosage on degradation efficiency of CR (catalyst dosage: 0.2–0.4 g, initial CR concentration: 8 mg L^{-1}, solution: 100 mL).

degradation activity compared to other CR solutions at earlier stage of reactions. This result derives from the increase of adsorption percentage of CR molecules by a unit of catalyst weight. In addition, a dilute CR solution with light color is able to enhance light utilization efficiency. The photocatalytic degradation rates for different amounts of CR under UV irradiation for 100 min are in following order: 100% (6 mg L^{-1}) > 99.9% (8 mg L^{-1}) > 98.7% (4 mg L^{-1}) > 98.4% (10 mg L^{-1}) > 95.8% (2 mg L^{-1}). Therefore, an optimum initial dye concentration of 6 mg L^{-1} is beneficial to thorough degradation of CR due to the strong synergistic effect between the adsorption of dye and the oxidation reaction of hydroxyl free radicals [34].

3.2.3. Degradation activities of different catalysts

Fig. 10 shows the degradation activities of different catalysts for CR. In order to know about the activities such as photocatalytic degradation, adsorption and photolysis, some experiments are designed as below. Both photocatalytic degradation for the Fe-immobilized catalysts and the removal of color tests for the Na-ASCM are carried out in an aqueous CR solution with suspending catalyst particles under UV irradiation in Fig. 10a–d. The adsorption experiment is about the aqueous CR solution with

solution suspending of 0.4 g of 5Fe$_2$O$_3$/ASCM catalyst as shown in Fig. 9. A rapid initial degradation rates take place for all of the CR dyes in the first 25 min, then slow down and finally reach equilibrium at 100 min. The CR dyes of 2 mg L^{-1} show the highest
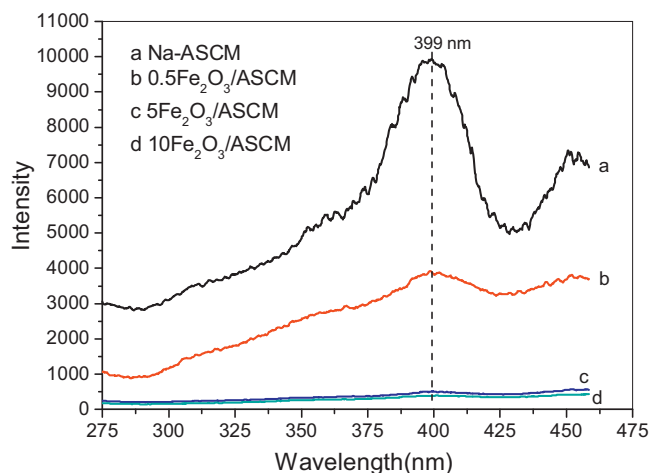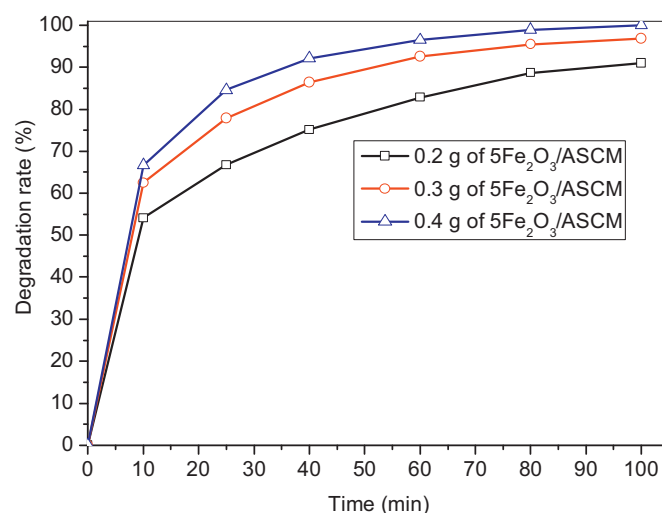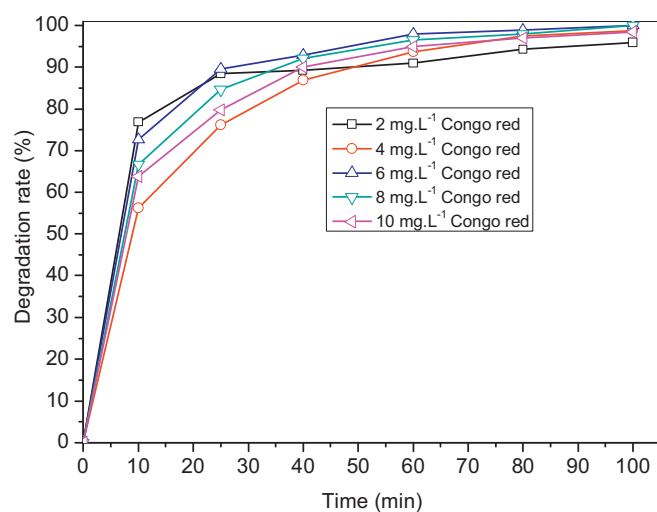

Fig. 9. Effect of initial dye concentration on degradation efficiency of CR (catalyst dosage: 0.4 g of 5Fe$_2$O$_3$/ASCM, initial CR concentration: 2–10 mg L^{-1}, solution: 100 mL).
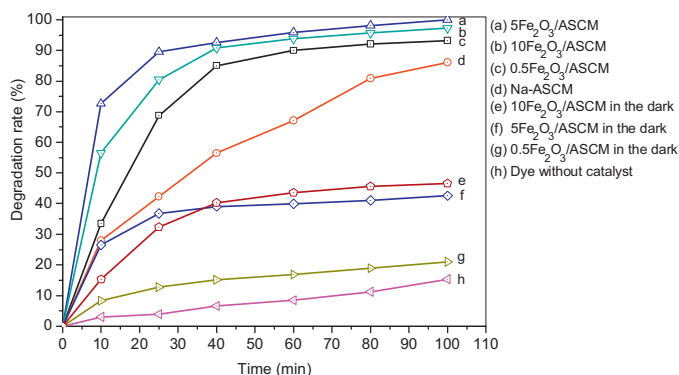
Fig. 10. Degradation activities of different catalysts for CR (composite dosage: 0.4 g, initial CR concentration: 6 mg L^{-1}, solution: 100 mL).

suspending catalyst is put in the dark in Fig. 10e–g. The photolysis test involves that the aqueous CR solution is exposed to UV light in Fig. 10h. It can be found from Fig. 10a that a series of Fe$_2$O$_3$/ASCM catalysts show excellent photocatalytic degradation rate in following order: 100% (5Fe$_2$O$_3$/ASCM) > 97.3% (10Fe$_2$O$_3$/ASCM) > 93.2% (0.5Fe$_2$O$_3$/ASCM) > 86% (Na-ASCM). As compared with Na-ASCM, higher activities for the Fe$_2$O$_3$/ASCM catalysts are considered to be the results of strong interaction between active species of Fe$_2$O$_3$ clusters and ASCM. The highest photocatalytic degradation rate for the 5Fe$_2$O$_3$/ASCM catalyst is probably ascribed to the fact that the 5Fe$_2$O$_3$/ASCM catalyst has the lowest absorption intensity in the near infrared region in Fig. 6, and the active species of Fe$_2$O$_3$ clusters dispersed homogeneously on the ASCM surface in Fig. 5 provides much more effectively active sites to promote the photocatalytic degradation reaction. Lower remove efficiency for the Na-ASCM probably results from that the CR dyes having sulfonate groups (CR-SO$_3^-$) with negative charges are strongly adsorbed on the Na$^+$ sites of the Na-ASCM via an electrostatic interaction. The adsorption results list as below: 46.5% (10Fe$_2$O$_3$/ASCM) > 42.5% (5Fe$_2$O$_3$/ASCM) > 21.0% (0.5Fe$_2$O$_3$/ASCM), suggesting that the removal rate of CR is in proportion to the Fe$_2$O$_3$ loading. It can be observed that the aqueous CR solution shows the lowest photolysis rate of 15.3%.

Fig. 11 shows the UV–vis absorption spectra of samples. The absorption spectrum of 6 mg L^{-1} solution of CR shows two bands

Fig. 11. UV–vis spectra of samples: (a) aqueous solution of CR dye, (b) aqueous solution of Fe$_2$O$_3$ sample, (c) aqueous solution of 5Fe$_2$O$_3$/ASCM sample, (d) aqueous solution of 5Fe$_2$O$_3$/ASCM after degradation for 100 min and (e) aqueous solution of ASCM sample.
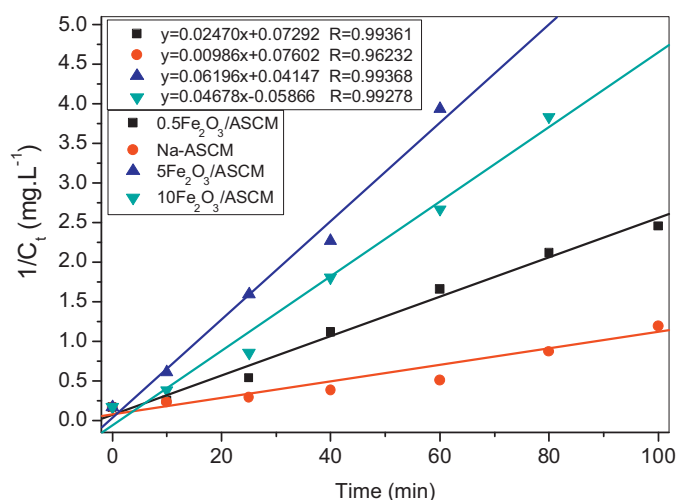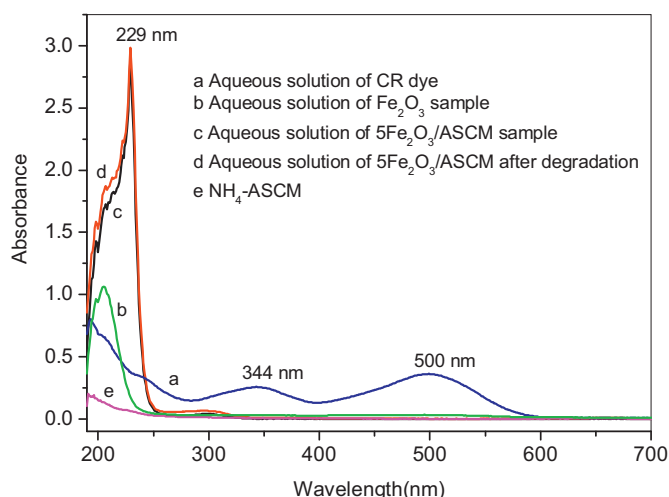

Fig. 12. Reaction kinetics of photocatalytic degradation of CR.

which one is in the visible region with maximum absorption at 500 nm and the other is in the ultraviolet region at 344 nm in Fig. 11a. It is assigned to be the band at 500 nm for azo bonds and the band at 344 nm for benzene, naphthalene rings in the CR molecule [35]. After the photocatalytic degradation of CR in the solutions suspending a solid Fe$_2$O$_3$/ASCM catalyst for 100 min, the absorption peaks of degradation products almost completely disappear in the range of 254–600 nm in Fig. 11d, demonstrating that the conjugated part, azo moieties and some naphthalene rings in the molecule are destroyed. It is known that the hydroxyl radical (•OH) is the major oxidative intermediate to react with azo moieties in high rate coefficients [36].

To understand whether the sharp peak at 229 nm in Fig. 11d originates from the residual fragment of dye or not, three kinds of contrast tests are done, which involve 5Fe$_2$O$_3$/ASCM, NH$_4$-ASCM and Fe$_2$O$_3$ samples to be put into water for 100 min and then carries out centrifugal separation, respectively. It can be found that the UV–vis spectrum of aqueous solution for the 5Fe$_2$O$_3$/ASCM sample in Fig. 11c is almost overlapping with 5Fe$_2$O$_3$/ASCM sample after degradation in Fig. 11d. There are a middle of peak for Fe$_2$O$_3$ sample in Fig. 11b and no peak for NH$_4$-ASCM sample in Fig. 11e. Therefore, it can be taken into account that the peak at 229 nm in Fig. 11d is closely associated with the strong interaction between Fe$_2$O$_3$ and ASCM, and also probably contains a small amount of aromatic fragments degraded from CR molecules comparing with Fig. 11a.

3.3. Kinetics of photocatalytic degradation of CR

To know the kinetics of photocatalytic degradation of CR in the solutions suspended on different solid Fe$_2$O$_3$/ASCM in Fig. 10, different kinds of kinetics orders are attempted to express the reaction kinetics as shown in Table 3. Each correlation coefficient was calculated from the kinetics equation, where R_0, R_1, R_2 and R_3 represent the correlation coefficients of zero, first, second and third order rate equations, respectively. Comparison with these correlation coefficients it can be found that the R_2 has the best correlation in the range of 0.96232–0.99368 for the different catalysts in Table 3. Therefore, it is suggested that the photocatalytic degradation of CR in the solutions suspended on solid Fe$_2$O$_3$/ASCM composite belongs to second order reaction kinetics as shown in Fig. 12. From Table 3 it is seen that the k$_2$, rate constant of second order reaction kinetics, has a positive order as below: 0.06196 (5Fe$_2$O$_3$/ASCM) > 0.04678 (10Fe$_2$O$_3$/ASCM) > 0.02470 (0.5Fe$_2$O$_3$/ASCM) > 0.00986 (Na-ASCM), and also the $t_{1/2}$,

Table 3
Kinetics equation of photocatalytic degradation of CR.

Composite	Order (s)	k_2 (L mg^{-1} min^{-1})	R_0	R_1	R_2	R_3	$t_{1/2}$ (min)
Na-ASCM	$1/C_t = 0.00986t + 0.07602$	0.00986	−0.95547	0.99628	0.96232	0.89781	16.90
0.5Fe$_2$O$_3$/ASCM	$1/C_t = 0.0247t + 0.07292$	0.02470	−0.84493	0.95157	0.99361	0.97715	6.75
5Fe$_2$O$_3$/ASCM	$1/C_t = 0.06196t + 0.04147$	0.06196	−0.70518	0.95592	0.99368	0.831	2.69
10Fe$_2$O$_3$/ASCM	$1/C_t = 0.04678t - 0.05866$	0.04678	−0.77545	0.96232	0.99278	0.87989	3.56

half-life, has a negative order as below: 2.69 (5Fe$_2$O$_3$/ASCM) < 3.56 (10Fe$_2$O$_3$/ASCM) < 6.75 (0.5Fe$_2$O$_3$/ASCM) < 16.90 (Na-ASCM). These are in agreement with the results of photocatalytic degradation of CR in Fig. 10.

3.4. Mechanism of photocatalytic oxidative degradation

A possible mechanism for photocatalytic oxidative degradation of CR is put forward in Fig. 13. Congo red, 1-naphthalenesulfonic acid-3,3′-(4,4′-biphenylene bis (azo)) bis (4-amino-) disodium salt, is a benzidine-based anionic diazo dye. In the aqueous solution, this anionic diazo dye dissolves and ionizes out an anion of sulfonate group (for short CR-SO$_3^-$) as shown in Eq. (2).

$$CR\text{-}SO_3Na \xrightarrow{H_2O} CR\text{-}SO_3^- + Na^+ \tag{2}$$

The Fe$_2$O$_3$ covered on the surface of CSH and CAH in the form of clusters is a semiconductor with a narrow bandgap about 1.9 eV deriving from Fig. 6c. Gulshan et al. [37] reported that the iron oxides of maghemite and hematite show semiconductor properties and have the activities of photodecomposition of methylene blue dye by UV, visible and solar radiation. As the Fe$_2$O$_3$ particles is irradiated by a beam of UV light, an electron in the VB acquires the energy of a photon to become a photogenerated electron (e$^-$) which migrates to CB and simultaneously leaves behind a photogenerated hole (h$^+$) in the VB as shown in Eq. (3) and Fig. 13.

$$Fe_2O_3 \xrightarrow{h\nu} Fe_2O_3(h^+) + e^- \tag{3}$$

The negative charges of AlO$_4$ tetrahedra located on the Si–O–Al framework of CSH gel are balanced by positive charges of Ca^{2+} ions [8,9]. CR dyes are more preferentially adsorbed on the surface-exposed Ca^{2+} sites due to stronger interaction between cationic Ca^{2+} and anionic sulfonate groups (CR-SO$_3^-$) as shown in Fig. 13. In tetrahedral co-ordination, Al^{3+} and Si^{4+} have radii of 0.39 and 0.26 nm respectively [38]. In addition, Si^{4+} possesses a Z/r (charge density) more than twice that of Al^{3+}, and strongly polarizes the electron density on its neighboring oxygen atom [1] so that Al^{3+} ions in framework of CSH shows a Lewis acidity which is able to provide unoccupied orbital acting as electron traps to ensnare photogenerated electron (e$^-$) in Fig. 13. The photogenerated hole (h$^+$) at the VB migrates to the surface of Fe$_2$O$_3$ clusters and reacts with

H$_2$O molecule to produce hydroxyl radical for the photocatalytic oxidation of dyes in Eq. (4) [39,40].

$$h^+ + H_2O \rightarrow H^+ + {}^\bullet OH \tag{4}$$

The anion of sulfonate groups (CR-SO$_3^-$) adsorbing on the surface of catalyst are oxidized by hydroxyl radicals to form the degradation products as shown in Eq. (5). The hydroxyl radical (${}^\bullet$OH) can successively participate in the oxidation reactions to make CR complete degradation.

$$CR\text{-}SO_3^- + {}^\bullet OH \rightarrow \text{Degradation products} \tag{5}$$
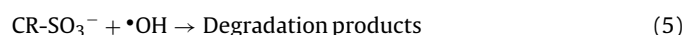
4. Conclusions

A new type of catalyst, ASCM loaded different amount of Fe$_2$O$_3$, was prepared via three-step route of polymerization, ion exchange and impregnation. FESEM results showed that the ASCM has a compact morphology with mean particle size about 50 nm. XRD results indicated that the CSH and CAH are main hydration products. The intensity of photoluminescence spectra precipitously decline due to the recombination probabilities of photogenerated electron–hole pairs to be effectively improved by enhancement of Fe$_2$O$_3$ content. High degradation activities for a set of Fe$_2$O$_3$/ASCM catalysts can be attributed to the strong interaction between ASCM and active species of Fe$_2$O$_3$. The dye anion of sulfonate groups (CR-SO$_3^-$) preferentially adsorbed on the Lewis acidity of Al^{3+} and Bronsted acidity of bridging hydroxyl group on the Si–O–Al framework of ASCM, and then was oxidized degradation by the hydroxyl radicals. The simulation result showed that the photocatalytic degradation of CR in the solution suspended on solid Fe$_2$O$_3$/ASCM catalyst is quite coincident with second order reaction kinetics.

References

[1] E.M. Gartner, D.E. Macphee, Cement and Concrete Research 41 (2011) 736–749.
[2] T. Bakharev, J.G. Sanjayan, Y. Cheng, Cement and Concrete Research 29 (1999) 113–120.
[3] S.A. Bernal, R.M. de Gutierrez, A.L. Pedraza, J.L. Provis, E.D. Rodriguez, S. Delvasto, Cement and Concrete Research 41 (2011) 1–8.
[4] G. Habert, J.B. d'Espinose de Lacaillerie, N. Roussel, Journal of Cleaner Production 19 (2011) 1229–1238.
[5] D. Roy, Cement and Concrete Research 29 (1999) 249–254.
[6] S.-D. Wang, X.-C. Pu, K.L. Scrivener, P.L. Pratt, Advances in Cement Research 7 (1995) 93–102.
[7] F. Pacheco-Torgal, J. Castro-Gomes, S. Jalali, Construction and Building Materials 22 (2008) 1305–1314.
[8] P. Duxson, J.L. Provis, Journal of the American Ceramic Society 91 (2008) 3864–3869.
[9] W. Mozgawa, J. Deja, Journal of Molecular Structure 924–926 (2009) 434–441.
[10] S. Song, H.M. Jennings, Cement and Concrete Research 29 (1999) 159–170.
[11] S. Song, D. Sohn, H.M. Jennings, T.O. Mason, Journal of Materials Science 5 (2000) 249–257.
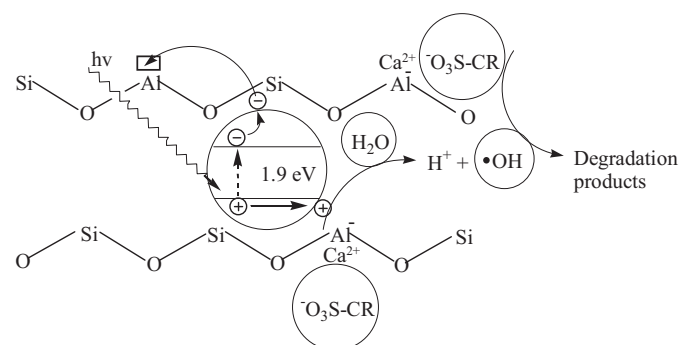[12] S. Wang, K.L. Scrivener, Cement and Concrete Research 25 (1995) 561–571.

Fig. 13. A mechanism of photocatalytic degradation of CR.

[13] A. Palomo, M.W. Grutzek, M.T. Blanco, Cement and Concrete Research 29 (1999) 1323–1329.
[14] S. Wang, K.L. Scrivener, Cement and Concrete Research 33 (2003) 769–774.
[15] F. Pacheco-Torgal, J. Castro-Gomes, S. Jalali, Construction and Building Materials 22 (2008) 1315–1322.
[16] C.K. Yip, G.C. Lukey, J.S.J. van Deventer, Cement and Concrete Research 35 (2005) 1688–1697.
[17] Y.J. Zhang, Y.C. Wang, D.L. Xu, S. Li, Materials Science and Engineering A 527 (2010) 6574–6580.
[18] C. Shi, Cement and Concrete Research 26 (1996) 1789–1799.
[19] D.M. Roy, W. Jiang, M.R. Silsbee, Cement and Concrete Research 30 (2000) 1879–1884.
[20] G. Qian, D.D. Sun, J.H. Tay, Journal of Hazardous Materials B 101 (2003) 65–77.
[21] J.W. Cho, K. Ioku, S. Goto, Advances in Cement Research 11 (1999) 111–118.
[22] J. Deja, Cement and Concrete Research 32 (2002) 1971–1977.
[23] G. Qian, D.D. Sun, J.H. Tay, Cement and Concrete Research 33 (2003) 1251–1256.
[24] G. Qian, D.D. Sun, J.H. Tay, Cement and Concrete Research 33 (2003) 1257–1262.
[25] Y.J. Zhang, L.C. Liu, Y. Xu, Y.C. Wang, D.L. Xu, Journal of Hazardous Materials 209-210 (2012) 146–150.
[26] P. Sazama, O. Bortnovsky, J. Dedecek, Z. Tvaruzkova, Z. Sobalik, Catalysis Today 164 (2011) 92–99.
[27] P. Duxson, A. Fernandez-Jimenez, J. Provis, G. Luke, A. Palomo, J.S.J. Van Deventer, Journal of Materials Science 42 (2007) 2917–2933.
[28] M.B. Haha, G.L. Saout, F. Winnefeld, B. Lothenbach, Cement and Concrete Research 41 (2011) 301–310.
[29] Y.J. Zhang, A. Maroto-Valiente, I. Rodriguez-Ramos, Q. Xin, A. Guerrero-Ruiz, Catalysis Today 93-95 (2004) 619–626.
[30] D.S. Perera, J.D. Cashion, M.G. Blackford, Z. Zhang, E.R. Vance, Journal of the European Ceramic Society 27 (2007) 2697–2703.
[31] L. Li, S. Wang, Z. Zhu, Journal of Colloid and Interface Science 300 (2006) 52–59.
[32] Y.J. Zhang, H.H. Li, Y.C. Wang, D.L. Xu, Advanced Materials Research 374-377 (2012) 1481–1484.
[33] W. Chen, Y. Xu, Z. Lin, Z. Wang, L. Lin, Solid State Communications 105 (1998) 129–134.
[34] C.C. Liu, Y.H. Hsieh, P.F. Lai, C.H. Li, C.L. Kao, Dyes and Pigments 68 (2006) 191–195.
[35] J. Wang, R.H. Li, Z.H. Zhang, W. Sun, R. Xu, Y.P. Xie, Z.Q. Xing, X.D. Zhang, Applied Catalysis A 334 (2008) 227–233.
[36] L. Flamigni, S. Monti, Journal of Physical Chemistry 89 (1985) 3702–3707.
[37] F. Gulshan, S. Yanagida, Y. Kameshima, T. Isobe, A. Nakajima, K. Okada, Water Research 44 (2010) 2876–2884.
[38] R.D. Shannon, Acta Crystallographica Section A 32 (1976) 751–767.
[39] M.A. Valenzuela, P. Bosch, J. Jimenez-Becerrill, O. Quiroz, A.I. Paez, Journal of Photochemistry and Photobiology A 148 (2002) 177–182.
[40] L. Zhang, X. Zhou, X. Guo, X. Song, X. Liu, Journal of Molecular Catalysis A: Chemical 335 (2011) 31–37.